RSC Advances

PAPER

View Article Online
View Journal | View Issue

Cite this: *RSC Adv.*, 2025, **15**, 40311

Desferrioxamine mesylate encapsulated novel chitosan based polymeric nanocomposites: insights into drug interaction, biocompatibility, cytotoxicity, cell permeability, antioxidant and controlled release properties

A. K. D. V. K. Wimalasiri,[a] P. Kalansuriya, *[a] B. P. Espósito,[b] T. A. Pereira,[b] Yongmei Zhao,[c] J. C. Godevithana,[d] K. Siriwardana,[e] M. Mohotti[f] and E. Lacerda[b]

Desferrioxamine (DFO) is a clinically established iron chelator used to manage iron overload in transfusion-dependent thalassemia patients. Despite its efficacy, DFO's poor cellular permeability and burst release profile limit its application to subcutaneous administration, precluding its use as an oral formulation. To address these limitations, DFO was encapsulated in a nanocomposite matrix composed of chitosan (CTS), polyethylene oxide (PEO), ethyl cellulose (EC), and tripolyphosphate (TPP). The resulting nanocomposites were comprehensively characterized using scanning electron microscopy (SEM), X-ray photoelectron spectroscopy (XPS), particle size analysis (PSA), and Fourier-transform infrared spectroscopy (FT-IR). The *in vitro* evaluation assessed drug release behavior at physiological pH, intestinal pH, and cellular uptake in HeLa cell lines. Among the tested formulations, DFO_PEO_EC_CTS_TPP_1 exhibited the highest drug loading capacity (285.56 ± 0.04 mg g^{-1}), entrapment efficiency (85.67 ± 13.35%), and antioxidant activity. Drug release kinetics were best described by the Peppas–Sahlin model (R^2 = 0.9999), indicating a Case II relaxation-controlled mechanism, supporting a sustained release profile. Blood compatibility was confirmed through Wilks' Lambda test, comparing coagulation parameters (APTT, PT) and complement levels (C3) between control and treated samples, including Fe(III)-DFO_PEO_EC_CTS_TPP_1 at 0.5 mg mL^{-1} and 37 °C. No statistically significant differences were observed (*e.g.*, PT, p = 0.052), confirming the hemocompatibility of the formulation. The MTT cytotoxicity assay for the optimal formulation yielded an IC_{50} value of 29.9 ± 5 μM, indicating acceptable cytocompatibility. Furthermore, the formulation demonstrated enhanced DFO permeability across cell membranes and sustained drug release over time. In conclusion, encapsulation of DFO within the PEO_EC_CTS_TPP nanocomposite matrix presents a promising strategy to overcome the limitations of native DFO, offering improved cell permeability, biocompatibility, and controlled release, potentially advancing it toward more effective therapeutic applications.

Received 21st June 2025
Accepted 10th October 2025

DOI: 10.1039/d5ra04417k

rsc.li/rsc-advances

Introduction

Iron overload is a secondary health complication associated with transfusion-dependent thalassemia. While increasing the quality of patient life and life expectations, complications silently induce life threatening situations in the body. When free iron species are accumulated in the cytoplasm, it will catalyze the production of free radicals *via* Fenton reaction. Consequently, DNA destruction and tissue damage occur ultimately leading to cell apoptosis.[1,2]

In order to reduce the iron burden in these patients, iron chelator desferrioxamine (DFO) is administered. The average daily dose of DFO is estimated to 20–60 mg per kg per day. Patients with serum ferritin levels of <2000 ng mL^{-1} should require about 25 mg per kg per day, and those with levels between 2000 and 3000 ng mL^{-1} about 35 mg per kg per day. In chronic situations, DFO is administered over a period of 8–12 hours each day.[3–5] On the other hand, patients with thalassemia major require lifelong regular blood transfusions usually every two to five weeks and this situation may intensify the iron overload (IO) in those patients.[6] However, certain drawbacks associated with

[a]*Department of Biochemistry, Faculty of Medicine, University of Ruhuna, Sri Lanka. E-mail: p_kalansuriya@med.ruh.ac.lk*
[b]*Department of Fundamental Chemistry, University of São Paulo, São Paulo, Brazil*
[c]*School of Pharmacy, Nantong University, China*
[d]*Department of Community Medicine, Faculty of Medicine, University of Ruhuna, Sri Lanka*
[e]*Department of Chemistry, Faculty of Science, University of Ruhuna, Sri Lanka*
[f]*Department of Haematology, National Hospital Galle, Karapitiya, Sri Lanka*

DFO make the drug not suitable for oral administration. The extreme hydrophilicity of DFO due to the presence of hydroxamine acid moieties tends to decrease the cell permeability while increasing the rate of excretion through urine, leading to a short plasma half-life of 5–10 min, which requires increased frequency of drug administration. Therefore, in order to obtain the maximum efficacy, DFO has to be infused *via* subcutaneous injection process in a continuous manner. However, subcutaneous administration of DFO is a tedious and painful process often leading to common local skin reactions.[7] Further, patients feel distressed for having to undergo chelation therapy. In addition, patients' life can become cumbersome without a supportive family, care giver nurses and *etc.* As this is a lifelong therapy it is important to find alternative options such as oral formulations leading to better patient compliance. However, the major challenge associated with the formation of oral formulation is its poor cell permeability. The present work discussed about the fabrication of DFO based nanochelators which entrap DFO for the purpose of achieving controlled release and enhance cell permeability property. Numerous studies related to the formation of DFO-based nanochelators have been reported.[8] Pharmacokinetic, cell toxicity and plasma half-life of the DFO encapsulated liposomes,[4,9–11] PEG–acrylate copolymer conjugated DFO,[5] DFO bile acid-targeted hyaluronic acid,[12] DFO incorporated natural polyphenols[13] have been studied in this regard. In order to fabricate a nanochelator which can scavenge DFO, it is worth to have a surface that facilitate the formation of van der Waals interactions with DFO and chitosan would be an excellent candidate for making this combination. Chitosan can improve the oral bioavailability of drugs by facilitating GI absorption.[14] On the other hand, few studies such as DFO incorporated chitosan,[15] chitosan_hyaluronic acid composite[16] and carboxymethyl_-chitosan derivatives,[17] have been reported so far to investigate the use of chitosan as an effective vehicle for DFO delivery. However, investigations of hydrophilic (CTS and PEO) and hydrophobic (EC) polymer hybrid blends on encapsulation of DFO and enhancement of cell permeability have not been investigated. Moreover, pH-dependent drug release ability of CTS, PEO and EC blended polymer composites have not been studied so far. Therefore, there is ample space to explore the use of CTS combinations with other polymer combinations for the controlled release of DFO and their effect on cell loading of DFO.

Considering these facts, novel hydrophilic and hydrophobic polymers blended DFO was synthesized using tripolyphosphate (TPP) crosslinked chitosan (CTS), ethyl cellulose (EC) and polyethylene oxide (PEO) aiming to increase the controlled release property and cell permeability. The synthesized composites were subjected to various *in vitro* assays to identify cell permeability, cell toxicity, blood compatibility, antioxidant and pharmacokinetics properties.

Materials and methods

Materials

Analytical grade chemicals were used in this study without any further purification. Desferrioxamine mesylate (95%) (DFO), ethyl cellulose (EC, ethoxyl content 48%), poly (ethylene oxide) (PEO, MW 600 000–1 000 000), chitosan (MW 600 000–800 000), sodium tripolyphosphate (TPP) and Tween 80 were purchased from Thermo Fisher Scientific. To screen blood compatibility, blood and plasma were obtained from healthy volunteer donors according to accepted and previously reported methods. PT (TEClot PT-S) and APTT (TEClot APTT-S) reagents were purchased from Ruhunu Hospital Pvt Ltd, Karapitiya. Human cervical carcinoma (HeLa) cells and salicylaldehyde isonicotinoyl hydrazone (SIH) were gifts from Prof. Esposito B., University of Sauo Paulo, Brazil and Dr Prem Ponka, McGill University, Canada respectively. Calcein-AM was gifted from Hayward, USA, (Biotium). Dimethyl sulfoxide (DMSO), ferrous ammonium sulphate (FAS), NaCl, sodium nitrilotriacetate (NTA), HEPES and (3-(4,5-dimethyl thiazol-2yl))-2,5 diphenyl tetrazolium (MTT reagent) were purchased from Sigma-Aldrich. Murine mammary carcinoma cells (4T1) were gifted from Yongmei Zhao, School of Pharmacy, Nantong University, China and dihydrorhodamine hydrochloride (DHR) was purchased from Biotium. HBS buffer-pH7.4 was prepared by mixing HEPES (20 mM) NaCl (150 mM) washed with Chelex (Sigma-Aldrich) (1 g/100 mL).

Synthesis of nanocomposites

Optimization of stabilizer (Tween 80%) percentage. A 1% solution of ethyl cellulose (EC) in ethyl acetate (EtOAc) (w/v) was prepared and sonicated until complete dissolution. Polyethylene oxide (PEO) was dissolved in two different stabilizer systems PEO_EC_1 (stabilizer: 50 mL of 0.4% Tween 80) and PEO_EC_2 (stabilizer: 50 mL of 0.2% Tween 80) with 0.1 g of PEO each. The organic phase was slowly injected into the stabilizer system (at 5 °C) while homogenizing the mixture (8000 U min^{-1}). After evaporating EtOAc, resulting white slurry was freeze dried, washed and characterized using PSA. Based on the PSA results, PEO_EC_1 was identified as the best system to synthesize smaller EC particles.

Preparation of DFO_PEO_EC_CTS_TPP nanocomposites using 0.4% Tween 80 stabilizer system. EC nanoparticles were synthesized using the optimized method as described above. A 1% (w/v) solution of ethyl cellulose (EC, 150 mg) in ethyl acetate (EtOAc) was prepared and sonicated until complete dissolution of EC. Polyethylene oxide (PEO, 150 mg) was dissolved in Tween 80 (0.4%, 75 mL). The organic phase was slowly injected into the stabilizer system (at 5 °C) while homogenizing the mixture (8000 U min^{-1}). *In situ* preparation of chitosan nanoparticles was carried out by mixing various amounts of chitosan (1% w/v) with the resulting white slurry. Briefly, 4 mL (system 1: PEO_EC_CTS_TPP_1), 2 mL (system 2: PEO_EC_CTS_TPP_2), 1 mL (system 3: PEO_EC_CTS_TPP_3), of chitosan (1% w/v) were added into the resulting white slurry (Table 1) and homogenized (8000 U min^{-1}, 15 min). To these mixtures, TPP (3% w/v) was added slowly at the ratio 2 : 5 (chitosan : TPP) and homogenized for 30 min at 8000 U min^{-1}. The resulting slurry was freeze dried and dialyzed using dialyzing tubing (D9777-100FT MEMBRANE-CEL MC 188100CLR), 3 L of deionized water for 72 hours to remove water-soluble components.

Table 1 Formula for the synthesis of different types of PEO_EC_CTS_TPP nanocomposites

Systems	EC weight (g)	PEO weight (g)	Volume of 1% (w/v) chitosan (mL)	Volume of 1% (w/v) TPP (mL)
PEO_EC_CTS_TPP_1	0.15	0.15	4.0	10.0
PEO_EC_CTS_TPP_2	0.15	0.15	2.0	5.0
PEO_EC_CTS_TPP_3	0.15	0.15	1.0	2.5

Loading of DFO to nanocomposites. An 80 mg portion of each freeze-dried sample was centrifuged (3000 rpm, 45 min) with DFO (40 mg, 2 mL). The DFO to composite ratio was maintained 1 : 2 (w/w). The resulting slurry was freeze-dried until a constant weight was obtained. The procedure was repeated for all three systems mentioned in Table 1 to form three formulations, DFO_PEO_EC_CTS_TPP_1, DFO_PEO_EC_CTS_TPP_2 and DFO_PEO_EC_CTS_TPP_3 (Fig. S1).

Analysis of surface charge and ζ potential of nanocomposites. The ζ potential was analyzed at three different pH values without loading DFO (1 mg in 10 mL). The pH 5.8, 6.5 and 7.4 were selected for the study in order to mimic the gastrointestinal and physiological pH conditions respectively. The nanocomposites (1 mg) were immersed in a buffer [0.01 M TBS at pH 7.4 and phosphate buffer 6.6 and 5.8] with the desired pH value for 24 hours and zeta potential was measured followed by analysis of surface charge.

Characterization of nanocomposites. Morphological studies of synthesized particles were conducted using scanning electron microscopy (Zeiss Gemini SEM 300600, at 15.0 kV). The presence of functional groups of synthesized particles was confirmed by analyzing FTIR spectra (Varian 660-IR) acquired in the wavenumber range of 500–4000 cm^{-1}. The bonding energy of certain elements of composite was analysed before and after loading DFO using the X-ray photoelectron spectroscopy (XPS). The XPS system (Thermo Fisher Scientific, UK) with X-ray source of Al Kα (1486.6 eV) equipped to an ultra-high vacuum chamber (base pressure better than 2×10^{-8} Pa) for the XPS measurements. XPS spectra of the survey with high pass energy (PE) and the core-level with low PE were done in the constant analyzer energy (CAE) mode with pass energy of 50–200 eV and energy step of 0.1 eV. The particle size was analyzed using PSA (Malvern, ver.7.2). The colloidal stability of the composite was measured using a Zetasizer (Malvern, ver.7.2). The amount of DFO loaded into composites was measured by potentiometric titration.

Determination of drug loading capacity (LC) and drug entrapment efficiency (EE %) of nanocomposites. The amount of DFO encapsulated in nanocomposites was quantified by using the standard assay procedure mentioned in the British pharmacopeia,[18] using potentiometric titration method. Briefly, 9 mg of DFO loaded PEO_EC_CTS was added into cellulose membrane dialysis tubing and 2 mL of deionized water was injected. The tubing was immersed in 50 mL of distilled water for five days. A 25 mL portion was taken and mixed with sulphuric acid (0.05 M, 4 mL). Finally, the mixture was titrated with 0.01 M ferric ammonium citrate. The end point was determined potentiometrically using platinum indicator electrode and a calomel reference electrode. The drug loading and drug entrapment efficiency were calculated using eqn (1) and (2), respectively.

$$\text{Drug loading capacity} = \frac{\text{Weight of DFO in nanochelator(mg)}}{(\text{Weight of nanochelator(g)})} \quad (1)$$

$$\text{Drug entrapment efficiency} = \frac{\text{Weight of DFO in nanochelator(mg)}}{\text{Weight of DFO loaded(mg)}} 100\% \quad (2)$$

Pharmacokinetic studies

In order to monitor the DFO release profile, the release of DFO was monitored using potentiometric titration method at different time points (0.5 to 60 min) at two pH values (pH 5.8 and pH 7.4) using 100 mg of DFO_PEO_EC_CTS_TPP_1, DFO_PEO_EC_CTS_TPP_2, DFO_PEO_EC_CTS_TPP_3, and buffer solutions [pH 7.4, 0.01 M tris buffer solution, 50 mL and phosphate buffer solution pH 5.8, 0.01 M phosphate buffer, 50 mL]. The collected kinetic data were interpreted using seven kinetic models (Table 2 and S1), namely, zero-order model (eqn (3)),[19–21] first-order model (eqn (4)),[19–21] Higuchi model (eqn (5)),[19,22] Korsmere–Peppas model (eqn (6)),[19,21] Hopfenburg model (eqn (7) and (8)),[23,24] Weibull model (eqn (9)),[24,25] and Peppas–Sahlin model[23,26,27] (eqn (10) and (11)).

Blood compatibility analysis

The nanocomposite (PEO_EC_CTS_TPP_1) which showed the best pharmacokinetic properties was selected for blood compatibility assays. All the procedures that use blood and serum samples from volunteer donors were performed in accordance with all relevant national (General circular number: 01-30/2020, issued by Ministry of Health and Indegenous Medicine) and international policies and regulations that govern research involving human participants and also all the experiments were approved by the Ethics Review Committee at Faculty of medicine, University of Ruhuna (No: 2022-P-072, Date: 17.01.2023). Informed consents were obtained from human participants of this study.

Prothrombin time (PT) and activated partial thromboplastin time (APTT)

PT and APTT assays were performed on whole blood collected from ten doners. Blood was collected to citrate anticoagulated tube (9 : 1: blood : citrate). The specimen was centrifuged

Table 2 Kinetic models and parameters

Model	Equation	Parameters
Zero-order model	$Q_t = k_0 t3$	Q_t, amount of drug dissolved in time t (min); k_0, zero-order release constant expressed in units of concentration/time
First order model	$\log Q_t = \log Q_o - \frac{Kt}{2.303}$ (4)	Q_o, the initial concentration of drug; k, first order rate constant; t, time; Q_t, amount of drug dissolved in time t
Higuchi model	$Q_t = k_H t^{1/2}$ (5)	Q_t, amount of drug dissolved in time t; k_H, Higuchi constant
Korsmeyer–Peppas model	$\frac{M_t}{M_\infty} = Kt^n$ (6)	M_t, amount of drug released in time t; M_∞, total amount of drug that must be released at infinite time; k, kinetic constant; n, release exponent
Hopfenburg model	$\left[1 - \frac{M_t}{M_\infty}\right]^{1/n} = 1 - \frac{k_t}{C_0 a} t$ (7) Linearized form of the eqn (7) can be written as $\left[1 - \frac{M_t}{M_\infty}\right]^{1/n} = 1 - \frac{k_t}{C_o a} t$ (8)	M_t, amount of the drug released at the time t; $M_{\infty,}$ amount released at the infinite time; $M_t/M_{\infty,}$ fraction of the drug released; $k_{t,}$ erosion grade constant; C_0, initial [drug] in matrix (mg g^{-1}); a, system half thickness (radius) (μm)
Weibull model	$\log[-\ln(1-m)] = b \times \log(t - T_1) - \log a$ (9)	m, accumulated drug fraction; a, time scale of the process; T_1, location parameter representing the latency time of dissolution process; b, shape parameter
Peppas–Sahlin model	$\frac{M_t}{M_\infty} = k_1 t^m + k_2 t^{2m}$ (10) $\frac{R}{F} = \frac{k_2}{k_1} t^m$ (11)	m = Fickian diffusion exponent; t = time in minutes; k_1 = kinetic constants of Fickian drug release process; k_2 = kinetic constants of case II relaxation-based drug release process Relaxational (R) contribution, Fickian contributions (F)

(1500 rpm, 10 min). The resulting citrate anticoagulated platelet poor plasma (PPP) was used for the analysis of PT and APTT. The effect of DFO_PEO_EC_CTS_TPP_1, Fe(III) bound DFO_PEO_EC_CTS_TPP_1 and DFO on coagulation was examined by mixing PPP with the above material in cuvette-strips (at 37 °C, 30 min). The final concentration of DFO was kept at 0.5 mg mL^{-1} in PPP. The required amount of DFO_PEO_EC_CTS_TPP_1, Fe(III) bound DFO_PEO_EC_CTS_TPP_1 was calculated by keeping the DFO amount constant (0.5 mg mL^{-1}). For APTT assay, a 25 μl portion of above prepared sample was mixed with 25 μl of APTT reagent and incubated (37 °C, 3 min). In here, silicate is used as the clotting activator. Then, 25 μl of pre warmed $CaCl_2$ (0.0025 M, at 37 °C, 1–2 min) were added to it. The control experiments were performed without adding DFO into the normal blood. Each experiment was repeated at least twice. For PT assay, a 25 μl of PPP sample was mixed with 50 μl of PT reagent at 37 °C. The clotting times were recorded using TECO GmbH coagulation analyzer.

Complement activation

Complement activation studies were performed using serum samples isolated by whole blood from two donors. DFO_PEO_EC_CTS_TPP, Fe(III)_DFO_PEO_EC_CTS_TPP and DFO samples were mixed with serum at a ratio to get a final concentration of 0.5 mg mL^{-1}. The samples were incubated (37 °C, 1 h) and then the procedure was followed as described in the DlAgAM complement C3 assay. Briefly, a 4 μl of serum was mixed with buffer solution (250 μl, PEG buffer pH 7, sodium chloride and sodium azide). The mixture was incubated (at 37 °C for 5 min) and optical density was measured at 340 nm using spectrophotometer. Then, a 50 μl of antiserum (anti human complement C3 antiserum) was added and optical density was measured after the 5 min incubation period.

Red blood cell aggregation and hemolysis in whole blood

To determine the effect of DFO, DFO_PEO_EC_CTS_TPP and Fe(III)_DFO_PEO_EC_CTS_TPP on red blood cell (RBC) aggregation, EDTA-anticoagulated whole blood was incubated for 1 h at 37 °C with the composites to get the final DFO concentration of 0.5 mg mL^{-1}. The required amount of DFO_PEO_EC_CTS_TPP_1, Fe(III) bound DFO_PEO_EC_CTS_TPP_1 was calculated by keeping the DFO amount constant (0.5 mg mL^{-1}). After incubation and centrifugation (3400 rpm, 30 min). RBC was examined by transmitted bright field light microscope (Olympus_2plus). Microplate reader (Thermo Scientific Varioskan Lux) was used to measure haemolysis (λ_{max} = 540 nm).

Cytotoxicity study

A murine mammary carcinoma cells (4T1) were cultured in DMEM medium supplemented with PBS and 1% penicillin–streptomycin at 37 °C in a 5% CO_2 incubator. Cells were seeded in 96 well plates at 8000 cells per well and incubated (24 hours). DFO, Fe_DFO_PEO_EC_CTS_TPP_1 and DFO_-PEO_EC_CTS_TPP_1 were separately dissolved in dimethyl sulfoxide (0.1% DMSO). The 4T1 cells were exposed to varied concentrations of DFO [3.125, 6.25, 12.5, 25, 50 μM] for 24 hours. MTT reagent were added to each well and incubated [20 μL, 4 hours]. DMSO were added after removing the solution from each well and absorbance were measured at 570 nm using microplate reader (Bio-Tek Instruments Inc., USA). Cytotoxicity calculation formula: cell viability (%) = (OD treatment group − OD blank group/OD control group − OD blank group) × 100%. IC 50 values were calculated using nonlinear regression analysis (Prism 8.0, GraphPad Software Inc., La Jolla, CA).

Cell permeability study

Human cervical carcinoma (HeLa) cells were seeded in 96-well microplates and incubated (37 °C, 24 hours with 5% CO_2) prior to the experiment. They were then washed twice with 100 μl of buffer and incubated with 100 μl of acetomethoxy–calcein (CAL-AM; 0.5 μM in phenol red-free medium, 37 °C, 20 minutes) and 5% CO_2. After washing with 100 μl HBS, fluorescence was registered for approximately 20 min ($\lambda_{exc}/\lambda_{em}$ = 485/520 nm; BMG FluoStar Optima). Then, 2 μl of iron stock solution (8-hydroxyquinoline-iron(III) complex 125 μM in water) were added and the fluorescence was registered until signal stabilization. The cells were then treated with diethylenetriaminepentaacetic acid (DTPA) [10 μM in Hepes Buffered Saline (HBS)] to remove the remaining extracellular iron. After that, the cells were exposed to 2 μl of the suspension of the nanocomposites in buffer ($n = 3$), to attain a final concentration of 50 μM in DFO, and the fluorescence was registered for approximately 30 minutes. The difference between final fluorescence and fluorescence at the time of chelator addition (Δfluorescence) was calculated, and used as an indicator of the degree of cell availability from the different nanocomposites. Salicylaldehyde isonicotinoyl hydrazone (SIH, 50 μM) was used as a positive control while free DFO (50 μM) was used as comparison.

Antioxidant potential of nanocomposites

The influence of DFO encapsulated nanocomposites on the iron-dependent oxidation of ascorbate was studied. In here, ferric nitrilotriacetate [Fe(nta)] solution was prepared by mixing FAS and NTA (10 μM, 1 : 1 mole, 37 °C, 1 hour). Aliquots of [Fe(nta)] (10 μM, 10 μL) were transferred to 96-well flat bottom black microplates followed by DFO encapsulated nanocompostes (0–40 μM, 10 μL). Each well was treated with 180 μL of DHR (50 μM) and ascorbic acid (40 μM) in HBS solution. Fluorescence ($\lambda_{exc}/\lambda_{em}$) = 485/520 nm) was registered during 1 hour at 1 min intervals (FluoStar Optima equipment (BMG) and the slopes from 15 to 40 min were calculated.

Stability of nanocomposite

The best nanocomposite (DFO_PEO_EC_CTS_TPP_1) was used to conduct stability testing. In brief, the product was stored in −20 ± 5 °C freezer and observations were made at two different time points including initial and after 24 months for drug loading capacities and FTIR spectra were compared.

Results and discussion

DFO was encapsulated in nanocomposites synthesized using PEO, CTS and EC to address the challenges arising due to the extreme hydrophilicity of drug, DFO. The hydrophobic EC and hydrophilic CTS and PEO polymers make the whole nanocomposite amphipathic and would increase the cell permeability. The combined effect of these two properties would be an advantage to develop a cell permeable controlled released DFO modularity in future.

Formulation of DFO_PEO_EC_CTS_TPP nanocomposites

Optimization of stabilizer (Tween 80%) percentage. Nanoparticles of desirable size and PDI were synthesized by changing stabilizer concentration and in order to penetrate through the intestinal epithelial cell membrane, the diameter less than 200 nm is desirable.[28] In here, the size of the nanocomposites was obtained as 104.81 ± 15.47 nm and 432.57 ± 11.64 nm for PEO_EC_1 and PEO_EC_2 as shown in Table 3. The polydispersity indexes of PEO_EC_1 and PEO_EC_2 are 0.79 ± 0.18 and 0.66 ± 0.11 respectively. Both the nanocomposites showed a size distribution from 10 nm to 1000 nm. Upon increasing the stabilizer concentration from 2% to 4%, by two-fold, a fourfold reduction of particle size was observed.

Based on the *Z* average and PDI, PEO_EC_1 synthesized using Tween 80 (0.4%) was selected for the synthesis of DFO_-PEO_EC_CTS_TPP nanocomposites. A milky dispersion of ethyl cellulose nanoparticles was obtained by non-solvent precipitation method. The prepared EC nanocomposites were fabricated by adding cationic polymer CTS in different ratios. Moreover, in order to fix the EC nanoparticles in CTS mesh, 3% (W/V) TPP was used at the ratio CTS : TPP 2 : 5. Finally, the three different types of DFO-encapsulated PEO_EC_CTS_TPP formulations were prepared by loading DFO.

DFO binding nature to PEO_EC_CTS_TPP : XPS based interpretation. XPS analysis was conducted to support the encapsulation of DFO into PEO_EC_CTS nanocomposite. In this study, wide XPS spectra of DFO, PEO_EC_CTS and DFO_-PEO_EC_CTS were measured in order to perform elemental identification as well as quantity of a detected element which can be estimated using the intensity of the corresponding photoelectron peak in a wide XPS spectrum. It allows the

Table 3 *Z*-average and PDI of different PEO_EC systems

System	*Z* average (nm)	PDI
PEO_EC_1 (EC 1)	104.81 ± 15.47	0.79 ± 0.18
PEO_EC_2 (EC 2)	432.57 ± 11.64	0.66 ± 0.11

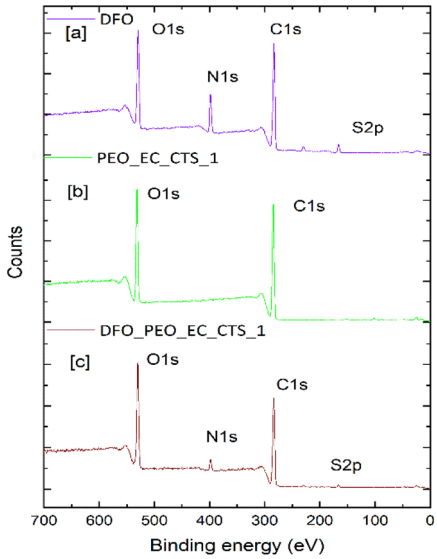

Fig. 1 XPS survey spectra of (a) DFO (b) PEO_EC_CTS_1 and (c) DFO_PEO_EC_CTS_1.

determination of the atomic composition of the selected elements in the sample before and after incorporating DFO.

Fig. 1 shows the XPS survey spectra of DFO, PEO_EC_CTS_1 and DFO_PEO_EC_CTS_1. The survey spectrum of DFO and DFO_PEO_EC_CTS_1 reveals the photoelectrons lines and the auger electron lines from mainly the elemental composition of C, N, S and O. The appearance of N 1s peak for primary amine group of CTS is not clearly shown in PEO_EC_CTS_1 composite. This is mainly due to the occurrence of low atomic N composition in the composite. However, N 1s and S 2p photoelectron lines are clearly visible in the XPS spectra (Fig. 1(c)) with the DFO encapsulation to the PEO_EC_CTS_1. It confirms the successful incorporation of DFO.

The N : S ratio of neat DFO and DFO_PEO_EC_CTS_1 were estimated considering the intensities of photoelectron lines of N 1s and S 2p peaks at binding energies of 398 eV and 166 eV, respectively while N : C ratio of neat DFO, PEO_EC_CTS_1 and DFO_PEO_EC_CTS_1 were also calculated using the photoelectron lines of C 1s (283 eV) and N 1s (398 eV). In this case, photoelectron intensities were normalized by the corresponding values of photoabsorption cross sections[29] and inelastic mean free path[30] as shown in the eqn (12).[31–33]

$$\frac{[N]}{[S]} = \frac{\sigma_{S\ 2p(h\nu)}\lambda_{S\ 2p\ incomposites}}{\sigma_{N\ 1s(h\nu)}\lambda_{N\ 1s\ in\ composites}} \times \frac{I_{N\ 1s}}{I_{S\ 2p}} \quad (12)$$

The N : S composition ratios were estimated to be 4.76 and 3.41 in the case of DFO and DFO_PEO_EC_CTS_1, respectively. On the other hand, the N : C ratios were estimated to be 0.22, 0.00006 and 0.06 for the DFO, PEO_EC_CTS_1 and DFO_PEO_EC_CTS_1. In contrast to the DFO incorporation, the composition ratio of N : C in DFO_PEO_EC_CTS_1 has been increased significantly proving its encapsulation into to PEO_EC_CTS_1 composite. This result is consistent with the data obtained from EDX and FT-IR analyses, which will be discussed in detail later.

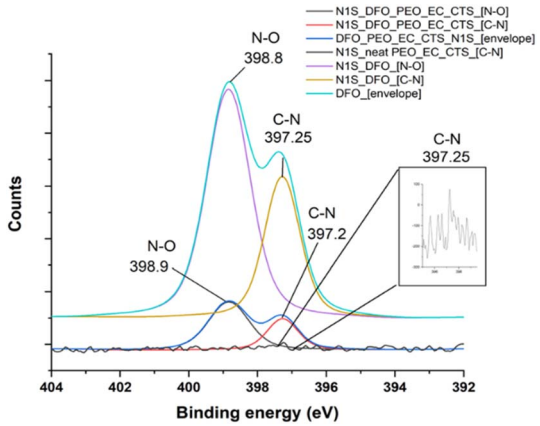

Fig. 2 Deconvolution of N 1s peak of DFO, PEO_EC_CTS_1 and DFO_PEO_EC_CTS_1.

In order to confirm the changes in each sub peak component, spectrums were deconvoluted (Fig. 2 and 3). Fig. 2 shows the deconvolution of N 1s peak of DFO, PEO_EC_CTS_1 and DFO_PEO_EC_CTS_1. The deconvolution of N 1s peak of DFO results two major sub peaks at 398.8 eV and 397.25 eV which were assigned to N–O and C–N, respectively. The photoelectron intensity for N 1s of primary amine attributed to PEO_EC_CTS_1 is very low and in the inset of Fig. 2 shows high resolution of N 1s peak of CTS amine. On contrary, the N 1s of DFO encapsulated PEO_EC_CTS_1 resolved into two sub peak confirming encapsulation of DFO further and that peaks appear

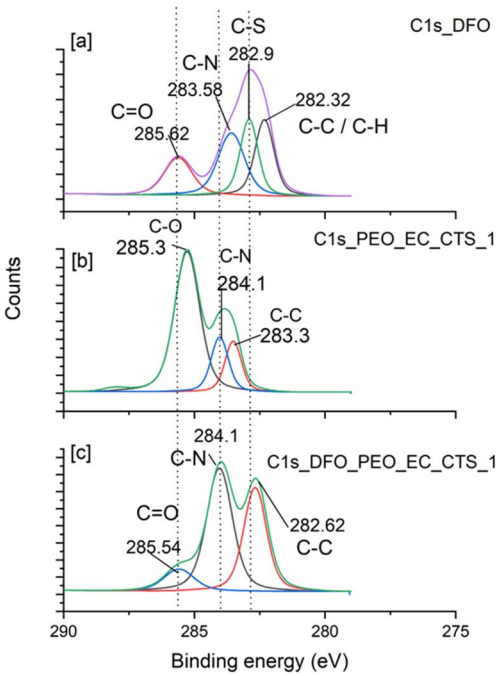

Fig. 3 Deconvolution of C 1s peak of (a) DFO, (b) PEO_EC_CTS_1 and (c) DFO_PEO_EC_CTS_1.

at 398.9 eV and 397.2 eV photoelectron lines. According to that, binding energy of N–O has increased by 0.1 eV upon interaction with the DFO. This result indicates that the positive charge around the N atom has increased. This may result due to the interaction of N atom of DFO with H of CTS, PEO or EC. However, the N 1s of C–N has shown very slight shift after binding with PEO_EC_CTS_1 (0.05 eV). The deconvolution of C1S DFO spectra comprised with four sub peaks at 285.6, 283.6, 282.9 and 282.3 eV which were assigned to C═O, C–N, C–S and C–C/C–H, respectively. Further, the deconvolution of C 1s peak of DFO_PEO_EC_CTS reveals three distinct sub peak 285.5, 284.1 and 282.6 eV which can be attributed to different environments: C═O, C–N and C–C, respectively. According to that, C 1s, C═O binding energy has been reduced by approximately 0.1 eV upon DFO binding to PEO_EC_CTS. The reason for this could be attributed to enhance hydrophobic environment around the carbonyl group. In this case, electron density of surrounding environment reduces the electron deficiency of the carbonyl carbon, causing a shift to lower binding energy. Electron density surrounding the C–N carbon of PEO_EC_CTS has not much changed due to the interaction with DFO. However, that for DFO (0.5 eV) has changed significantly upon binding with PEO_EC_CTS. The increased C 1s binding energy can be explained by depletion of electronic environment around C of C–N. For this to occur, nitrogen should form hydrogen bonds with surrounding hydrogen atoms of PEO_EC_CTS. This result is consistent with the XPS interpretation of N 1s of N–O. Based

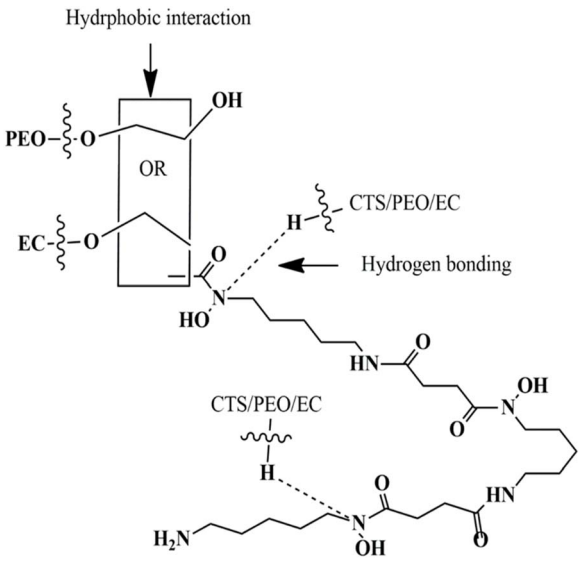

Fig. 4 Suggested structure for DFO_PEO_EC_CTS_TPP.

Table 4 Zeta potential at different pH values

pH	5.8 (mV)	6.5 (mV)	7.4 (mV)
PEO_EC_CTS_TPP_1	18.97 ± 2.44	9.53 ± 0.08	−2.95 ± 0.43
PEO_EC_CTS_TPP_2	18.53 ± 4.24	11.00 ± 0.29	−0.24 ± 0.14
PEO_EC_CTS_TPP_3	15.17 ± 5.15	8.82 ± 0.45	−1.68 ± 0.15

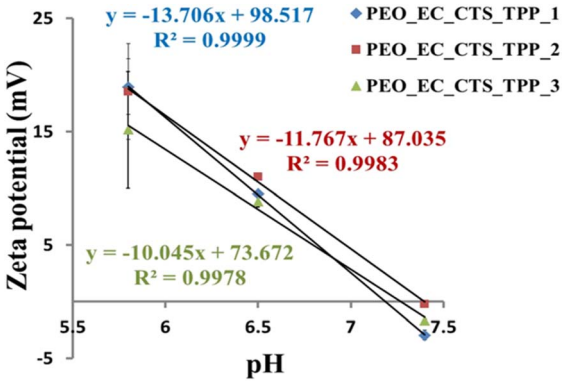

Fig. 5 Graphs of zeta potential *vs.* pH for all three formulations.

on the analysis of these results, two factors can be inferred. The major functional group involve in making interactions with PEO-EC-CTS is C–N–O. The major type of van der Waals interaction formed is hydrogen bonding, while hydrophobic interactions may also play a role in generating minor interactions.

The suggested structure for DFO binding to PEO_EC_CTS_TPP is shown in the Fig. 4. In here, the interaction between CTS (Fig. S2), EC and PEO with DFO would be mostly hydrogen bonding with N–O of DFO. These H bonding between PEO_EC_CTS_TPP and DFO would make the secured environment to keep the DFO in the nanocomposites.

In order to investigate the surface charge of the PEO_EC_CTS_TPP, ζ potential of all three formulations were analyzed before loading DFO and depicted in Table 4 at different pH values (pH 5.8, 6.5 and 7.4). The selected pH values would mimic the gastrointestinal and physiological pH conditions. Generally, zeta potential reveals the physical stability of colloidal suspension and provides an idea about the potential difference between the mobile dispersion medium and electric double layer attached to dispersed phase.

The Fig. 5 illustrates the variation of zeta potential with pH. According to that, the point of zero charge (pHpzc) of PEO_EC_CTS_TPP_1, PEO_EC_CTS_TPP_2 and PEO_EC_CTS_TPP_3 were 7.19 (±0.03), 7.39 (±0.11) and 7.31(±0.17) respectively. Hence it can be concluded that the nanocomposites are negatively charged at physiological pH value (7.4) and the zeta potential values were found to be −2.95 (±0.43), −0.24 (±0.14), −1.68 (±0.15) for PEO_EC_CTS_TPP_1, PEO_EC_CTS_TPP_2 and PEO_EC_CTS_TPP_3 respectively. On the other hand, zeta potential of PEO_EC_CTS_TPP_1, PEO_EC_CTS_TPP_2 and PEO_EC_CTS_TPP_3 at the pH 5.8 is 18.97 (±2.44), 18.53 (±4.24) and 15.17 (±5.15). It makes the surface positively charged at pH 5.8. Moreover, it was found that the zeta potential of all three nanocomposites at intestinal pH is not significantly different at 95% confidence interval. However, it was found that at pH 7, zeta potential values of three composites are significantly different and therefore the surface charges are also significantly different.

Characterization of DFO_PEO_EC_CTS nanocomposites

Morphological studies. Fig. 6 shows the SEM micrographs of (a) DFO_PEO_EC_CTS_TPP_1 (b) DFO_PEO_EC_CTS_TPP_2

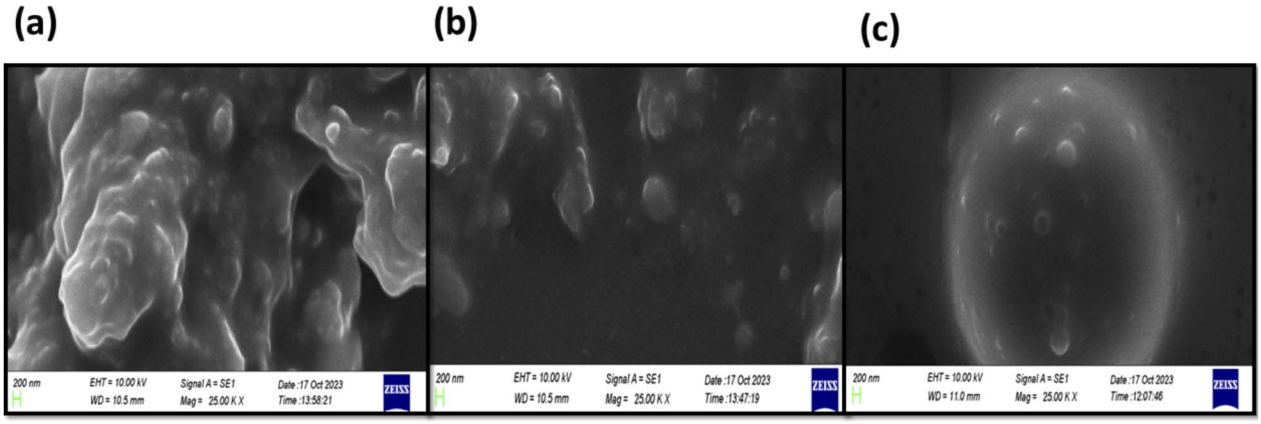

(d)

Elements	Atomic % of DFO incorporated PEO_EC_CTS_1	Atomic % of neat PEO_EC_CTS_1
C K	53.54	62.23
N K	12.59	7.18
O K	31.82	30.45
P K	0.48	0.10
S K	1.57	0.04

Fig. 6 SEM images of (a) DFO_PEO_EC_CTS_TPP_1 (b) DFO_PEO_EC_CTS_TPP_2 and (c) DFO_PEO_EC_CTS_TPP_3 (d) elemental composition of DFO_PEO_EC_CTS_TPP_1 and PEO_EC_CTS_TPP_1.

and (c) DFO_PEO_EC_CTS_TPP_3 (d) elemental distribution data of DFO_PEO_EC_CTS_TPP_1 and PEO_EC_CTS_TPP_1. As illustrated in Fig. 6(a) and (b) the shape of the DFO_-PEO_EC_CTS_TPP_1 particle is more irregular and morphology is polymeric in nature. This may be attributed to the high CTS content in the structure, as the polymeric nature decreased significantly with a reduction in CTS content. Fig. 6(c) indicates the morphological features DFO_PEO_EC_CTS_TPP_3 and it clearly shows the appearance of spherical shape particles of which is more similar to the EC particle morphology. Fig. S3 shows the elemental mapping data of DFO_-PEO_EC_CTS_TPP_1 in a selected portion of the composite and Fig. 6(d) indicates the surface elemental composition of DFO _PEO_EC_CTS_TPP_1 and PEO_EC_CTS_TPP_1. According to Fig. 6(d), the %N and %S of DFO _PEO_EC_CTS_TPP_1 is 12.59 and 1.57 while for PEO_EC_CTS_TPP_1 is 7.18 and 0.04, respectively. The increased %N and %S on surface is due to the contribution of amine and amide groups and mesylate groups of DFO (C26H52N6O11S). These results evidence the encapsulation of DFO into the neat matrix PEO_EC_CTS_TPP_1.

In order to determine the effect of CTS content on the size distribution, particle size analysis was conducted (Table 5) and this confirms the decrease in particle size with a reduction in CTS concentration, as well as the presence of polydispersity in all three formulations. In this case it was found that there are no significant differences in particles sizes at 95% confidence interval. However, as mentioned earlier, it was found that zeta potential values at pH 7.4 vary with increasing the CTS level and that is due to the cationic charges introduced by the CTS.

According to the FTIR spectra (Fig. 7), most of the prominent peaks specific to CTS, PEO and EC overlap with the peaks of DFO. Fig. 7(j) illustrates the FTIR spectrum of PEO and the peaks in spectrum are associated with number of vibrational modes. In this case, the broad peak appearing at 3474 cm^{-1} is attributed to the OH stretching of the polymer.[34] The sharp peak

Table 5 PSA data and polydispersity index (PDI) of synthesized nanocomposites

Nanocomposite	Particle size (nm)	PDI
DFO_PEO_EC_CTS_TPP_1	293.1 ± 52.9	0.79
DFO_PEO_EC_CTS_TPP_2	235.5 ± 48.1	0.68
DFO_PEO_EC_CTS_TPP_3	164 ± 39.5	0.43

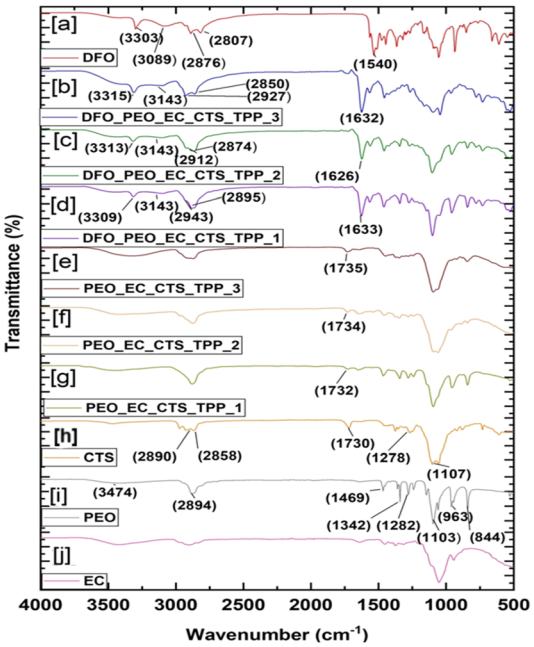

Fig. 7 FTIR spectra of (a) DFO (b) DFO_PEO_EC_CTS_TPP_3 (c) DFO_PEO_EC_CTS_TPP_2 (d) DFO_PEO_EC_CTS_TPP_1 (e) PEO_EC_CTS_TPP_3 (f) PEO_EC_CTS_TPP_2 (g) PEO_EC_CTS_TPP_1 (h) CTS (i) PEO (j) EC.

at 2894 cm^{-1} is related to the CH stretching mode.[34] The peak at around 1460 cm^{-1} corresponds to the asymmetric bending mode of CH_2.[34] The peaks present in the region from 1282 cm^{-1} to 1342 cm^{-1} are associated with CH_2 wagging and CH_3 bending.[34] The peaks at 844, 963 and 1103 cm^{-1} can be attributed to the CH_2 rocking, C–O–C vibrations mode and C–O–C stretching/–CH_2–CH_2 rocking, respectively.[34] Comparison of these results with Fig. 7(b–i) confirms the presence of PEO polymer as well on the particle. Moreover, when comparing sharpness and intensities of the peaks corresponding to CH_2 rocking (844 cm^{-1}) and C–O–C vibrations (963 cm^{-1}), an increasing trend in the aforementioned features was observed with higher chitosan levels in the composite.

The FTIR spectrum of CTS is shown in the Fig. 7(i) and according to that the most of the prominent peaks which are specific to CTS are overlapped with the peaks relevant to PEO and EC. Further, the peak attributed to the C=O stretching of amide in neat chitosan (1730 cm^{-1}) spectrum[33,35] has shifted to a higher wave number region in all composites due to hydrogen bond formation. In addition to that, the shifting of the peak position relevant to C=O stretching of amide bond in neat chitosan (1730 cm^{-1}) increase when decreasing the chitosan content of the composite. These results indicate that the formation of PEO_EC_CTS_TPP particles was successful.

The FTIR spectra of DFO and DFO encapsulated PEO_EC_CTS composites are shown in Fig. 7(a–d). The peak at 3303 cm^{-1} in Fig. 7(a) corresponds to the NH stretching vibration of the amine.[36] Further, the small peak at 3089 cm^{-1} is related to the C–N–H overtone.[36] The peak for the asymmetric CH_3 stretching vibration is at 2876–2807 cm^{-1}.[36] The peak at 1540 cm^{-1} can be attributed to the C=O stretching vibration.[36] Moreover, the peaks at 932–1048 cm^{-1} are related to the N–O stretching vibrations.[36] Post-adsorption characterization of the material was carried out using DFO encapsulated materials. The FTIR spectra of DFO-encapsulated systems are shown in Fig. 7(b–d). According to that, it can be clearly identified that characteristic peak positions of DFO start to shift when the DFO was added to the composites. For instance, the stretching band of DFO N–H (3303 cm^{-1}) appears at 3315 cm^{-1} in DFO_-PEO_EC_CTS_TPP_3 (Fig. 7(b)), 3313 cm^{-1} in DFO_-PEO_EC_CTS_ 2 (Fig. 7(c)), and 3309 cm^{-1} in DFO_PEO_EC_CTS_ 1 (Fig. 7(b)). This shift may occur due to the formation of hydrogen bonds in between NH of the DFO and OH groups of PEO, EC and CTS.[17,37] Further, the peak at 1540 cm^{-1} shifted significantly to 1632 cm^{-1} for DFO_-PEO_EC_CTS_TPP_3, to 1626 cm^{-1} for DFO_-PEO_EC_CTS_TPP_2, and to 1638 cm^{-1} for DFO_PEO_EC_CTS_TPP_1. The appearance of these prominent peaks related to DFO in all systems confirms the successful encapsulation of DFO on PEO_EC_CTS_TPP particles. Further, the identification of C–NH amide II stretching as well as N–O stretching peaks is difficult due to the overlaying of the peaks related to PEO, CTS and EC.

DFO_PEO_EC_CTS_TPP particles were treated with iron in order to ascertain if the iron binding affinity of DFO is intact. Fig. 8(a–c) shows FTIR spectra of Fe(III) bound DFO_-PEO_EC_CTS_TPP_3, DFO_PEO_EC_CTS_TPP_2 and DFO_-PEO_EC_CTS_1, respectively. Comparative to the metal-free composites, FTIR spectra of iron bound composites are very distinctive and confirm the chelation ability of the composites.

Drug loading capacities and drug encapsulation efficiency. The drug loading capacities of DFO_PEO_EC_CTS_TPP_1,

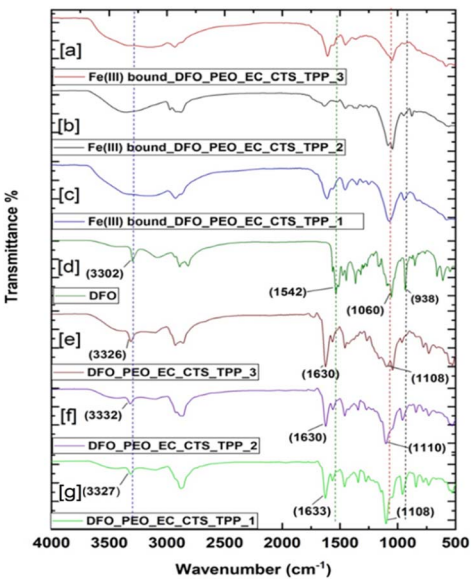

Fig. 8 FTIR spectra of (a) Fe(III) bound DFO_PEO_EC_CTS_TPP_3 (b) Fe(III) bound DFO_PEO_EC_CTS_TPP_2 (c) Fe(III) bound DFO_-PEO_EC_CTS_TPP_1 (d) DFO (e) DFO_PEO_EC_CTS_TPP_3 (f) DFO_PEO_EC_CTS_TPP_2 (g) DFO_PEO_EC_CTS_TPP_1.

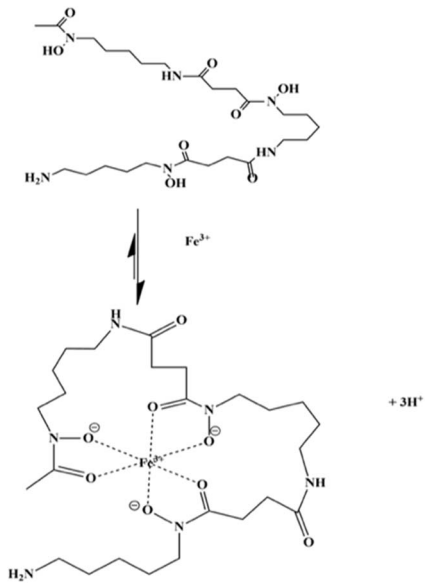

Fig. 9 Reaction between DFO and Fe(III) during potentiometric titration.

DFO_PEO_EC_CTS_TPP_2 and DFO_PEO_EC_CTS_TPP_3 were determined by potentiometric titration method (Fig. 9).

According to Table 6, the LC as well as EE increases with increasing the CTS content. This can be due to the increase of H bonding with increasing the CTS content.

Table 6 Drug loading capacity and drug entrapment efficiency of DFO_PEO_EC_CTS_TPP_1, DFO_PEO_EC_CTS_TPP_2, and DFO_PEO_EC_CTS_TPP_3

Nanocomposite	Drug loading capacity (mg g^{-1})	Drug entrapment efficiency (%)
DFO_PEO_EC_CTS_TPP_1	285.56 ± 0.04	85.67 ± 13.35
DFO_PEO_EC_CTS_TPP_2	193.58 ± 0.06	58.07 ± 16.95
DFO_PEO_EC_CTS_TPP_3	179.12 ± 0.05	53.74 ± 15.30

In vitro pharmacokinetic studies. The main purpose of loading DFO in PEO_EC_CTS_TPP matrix is to control the rate of DFO to enhance its retainment in blood/target tissue. DFO_-PEO_EC_CTS_TPP system should initially release part of the DFO dose in order to reach to the effective therapeutic concentration. Then the DFO release profile should follow a well-defined pattern to maintain the supplement dosage for the required period of time. To evaluate if the synthesized DFO encapsulated nanocomposite is effective in the controlled release platform and to predict the release kinetics *in vitro* before advancing to the pre-clinical stage, it is vital to study the release profiles of the novel DFO nanocomposites. Herein, a model dependent method was used to describe the DFO dissolution profile from DFO_PEO_EC_CTS_TPP. Goodness of fit was determined for each formulations using the models such as Higuchi model[19,22] Korsmeyer–Peppas model, zero order model,[19,20] Peppas–Sahlin model, Hopfenburg model, Weibull model[25] and first order (Fig. 10, S4 and S5).[19] According to the regression coefficient values (R^2) the dissolution profile of all three different formulations is well in agreement with the Peppas–Sahlin model at both pH values (Fig. 10). Generally, Peppas–Sahlin model is used to explain the dissolution profile of polymeric substances which shows anomalous drug release profile. In this case, approximate contributions of the diffusional and relaxational mechanisms in an anomalous drug release process is determined. The kinetic parameters and R^2 at two different pH values are summarized in Tables 7 and S2. According to that, the Fickian kinetic constant (k_1) for all three DFO_PEO_EC_CTS_TPP composites is zero at both values (pH 7.4 and 5.8). Comparatively, the kinetic constants of case II relaxation-based drug release process (k_2) are high for all the composites at both pH values (Table 7) suggesting case II relaxation is as most probable mechanism that predict DFO release. Further, R/F values for all the composites are greater than one at both pH values ($k_1 = 0$). Considering these results, it can be concluded that the release of DFO from the DFO_-PEO_EC_CTS_TPP_1 nanocomposite is governed by the case II relaxation. However, the determination of exact drug release mechanism for DFO_PEO_EC_CTS_TPP_3 is much complicated

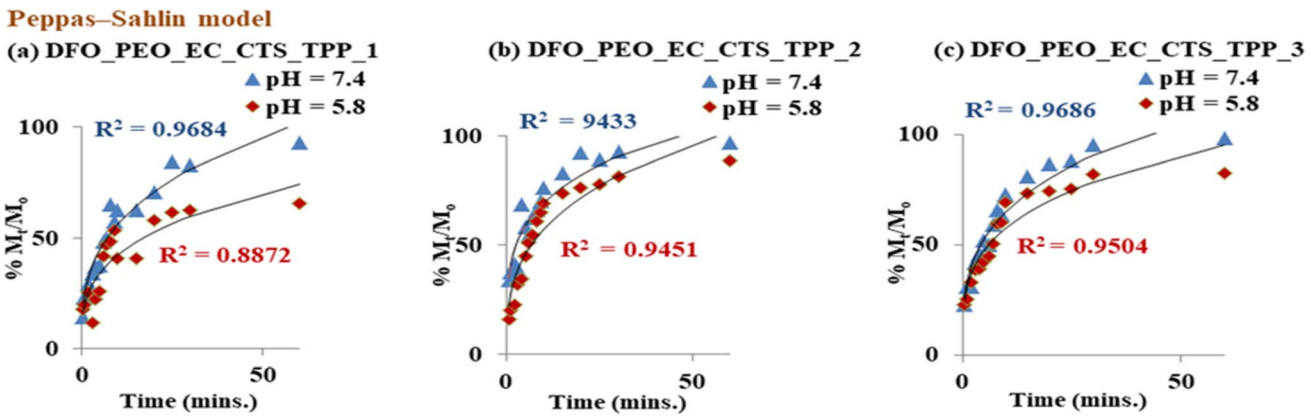

Fig. 10 DFO dissolution profiles of nanocomposites (a) DFO_PEO_EC_CTS_TPP_1 (b) DFO_PEO_EC_CTS_TPP_2 (c) DFO_PEO_EC_CTS_TPP_3.

Table 7 Kinetic parameters and correlation coefficients at two different pH values (Korsmeyer–Peppas model, Hopfenburg model, Weibull model and Peppas–Sahlin model)

Model	Korsmeyer–Peppas				Hopfenburg model				Weibull model				Peppas–Sahlin model							
pH	7.4		5.8		7.4		5.8		7.4		5.8		7.4				5.8			
Parameters	n	R^2	n	R^2	k μm mg g^{-1} min^{-1}	R^2	k μm mg g^{-1} min^{-1}	R^2	b	R^2	b	R^2	k_1 min^{-m}	k_2 min^{-2m}	m	R^2	k_1 min^{-m}	k_2 min^{-2m}	m	R^2
DFO_PEO_EC_CTS _TPP_1	0.4 ± 0.02	0.94	0.35 ± 0.03	0.71	0.34 ± 0.32	0.79	0.18 ± 0.06	0.63	0.6 ± 0.05	0.96	0.45 ± 0.05	0.73	0	25.9 ± 3.5	0.17 ± 0.006	0.96	0	20.44 ± 1.6	0.16 ± 0.006	0.89
DFO_PEO_EC_CTS_TPP_ 2	0.26 ± 0.024	0.89	0.42 ± 0.036	0.93	0.28 ± 0.22	0.79	0.22 ± 0.04	0.74	0.5 ± 0.09	0.9	0.6 ± 0.006	0.95	0	39.82 ± 3.2	0.12 ± 0.002	0.94	0	27.4 ± 3.3	0.16 ± 0.01	0.95
DFO_PEO_EC_CTS _TPP_3	0.33 ± 0.009	0.87	0.32 ± 0.01	0.91	0.15 ± 0.1	0.87	0.09 ± 0.42	0.69	0.57 ± 0.05	0.95	0.45 ± 0.05	0.94	0	39.8 ± 4.8	0.12 ± 0.01	0.97	0	27.4 ± 5.1	0.16	0.95

as it depends on the pH value of the system. Moreover, the Fig. S4(a–c) indicate the kinetic data fitted to the Higuchi model while the Fig. S4(d–f) shows the data fitted to zero-order kinetic model and it depicts the cumulative amount of drug release with time. Fig. S4(g–i) shows the data fitted to first-order kinetic model. Additionally, Fig. S5 shows the DFO dissolution profile of composites (a–c) Weibull model (d–f) Hopfenburg model (g–i) Korsmeyer–Peppas model. Comparing these results, it can be noted that the cumulative drug release is higher at the pH 7.4 than the pH 5.8. These results provide evidence for the pH responsive controlled release of DFO.

Controlled release behavior of DFO. In order to analyze the controlled release behavior of DFO, the percentage of DFO release was plotted against the incubation time. In general, conventional drug release profiles oscillates between maximum in plasma drug concentration (crest) and decrease (trough).[38] Hence, giving repeated dosage is necessary to maintain the plasma DFO concentration. On the other hand, as a burst release is shown at the beginning, in most of the conventional drug administrations, the initial plasma drug concentration is higher than the therapeutically effective level.[38] Therefore, it is imperative to deliver the drug at a required rate for a period of time to achieve the therapeutic level. Fig. 11 shows the sustained released pattern of DFO from nanocomposites at different pH conditions. According to the Fig. 11(a), at pH 7.4, the first 50% of DFO has been released within less than 10 min by DFO_PEO_EC_CTS_TPP_2 and DFO_PEO_EC_CTS_TPP_3 and within approximately 6 min by DFO_PEO_EC_CTS_TPP_1. This is an essential part in a controlled drug release platform as the plasma need to achieve the therapeutic level of the drug initially. In order to release rest of the encapsulated DFO, it has taken more than 120 minutes showing the sustained release pattern of DFO. On the other hand, Fig. 11(b) shows the drug dissolution profile of all three formulations at pH 5.8. Comparatively to the drug release profile at pH 7.4, the rate of DFO release is much slower at pH 5.8. In order to release the first 50% of DFO at pH 5.8 from DFO_PEO_EC_CTS_TPP_1 it has taken approximately 22 minutes and even after one hour it has released up to 60% of DFO. This is an advantage in oral drug formulation as it indicates a slower DFO release at the intestinal pH. Further, at intestinal pH, DFO_PEO_EC_CTS_TPP_2 and DFO_PEO_EC_CTS_TPP_3 composites have taken approximately 5 min to release 50% and more than two hours to release 90% of DFO.

Regarding drug release for cell therapy purposes (Fig. 12), as shown by the ability of DFO to scavenge iron from the intracellular calcein–iron complex and subsequent recovery of calcein fluorescence, DFO_PEP_EC_CTS_TPP_1, DFO_PEP_EC_CTS_TPP_2 and DFO_PEP_EC_CTS_TPP_3 were particularly able to load DFO into cells.

The cell permeability data were analyzed using one-way analysis of variance (ANOVA), followed by Turkey *post hoc* test, to determine statistically significant differences between the cell permeability of DFO and DFO encapsulated PEO_EC_CTS_TPP. The results show that of DFO_-PEO_EC_CTS_1 ($p = 0.041$) and DFO_PEO_EC_CTS_2 ($p = 0.033$) and DFO_PEO_EC_CTS_3 ($p = 0.01$) exhibit different cell

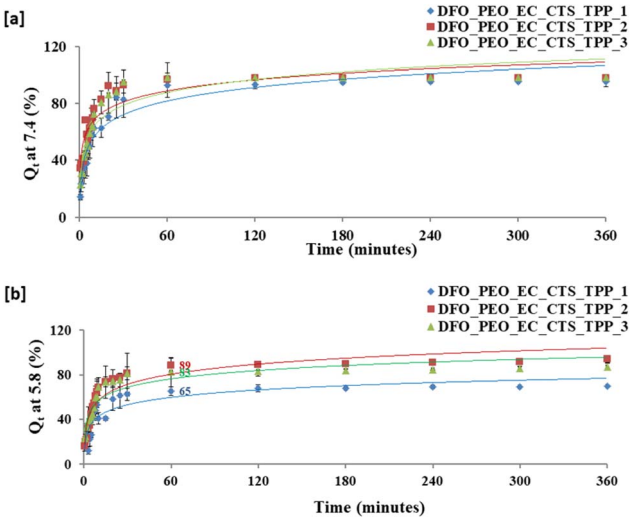

Fig. 11 Sustained drug release pattern of modified drug formulations (a) at pH 7.4 and (b) at pH 5.8.

permeability compared to DFO indicating that there is statistically significant difference in cell permeability. Considering these results, it can be concluded that the DFO binding to PEP_EC_CTS_TPP could improve the cell permeability of DFO. Moreover, the results indicate that DFO_PEO_EC_CTS_1, DFO_PEO_EC_CTS_2 and DFO_PEO_EC_CTS_3 exhibit similar cell permeability ($p = 0.413$) demonstrating that within the selected concentration range of CTS the cell permeability is not significantly different. These results support that the novel nanocomposites are promising candidates for the development of a controlled rerelease DFO drug modularity.

The cell permeability data was compared with the DFO release data at pH 5.8 and it was inferred that there is no significant correlation between cell permeability and DFO release rate of the composites.

***In vitro* blood compatibility assay.** The drug formulation with the highest drug encapsulation efficiency was used for the *in vitro* blood compatibility assays.

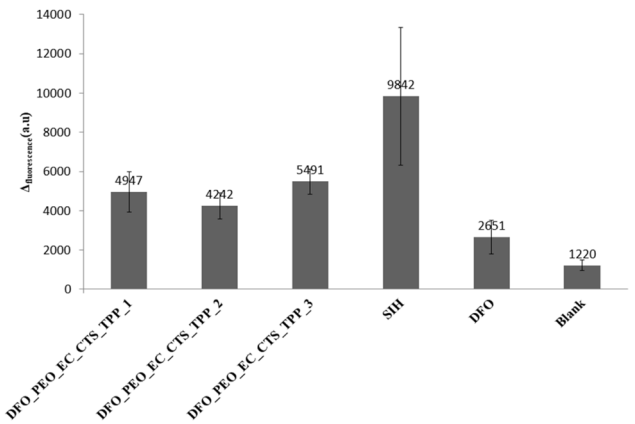

Fig. 12 Cell permeability of nanocomposites.

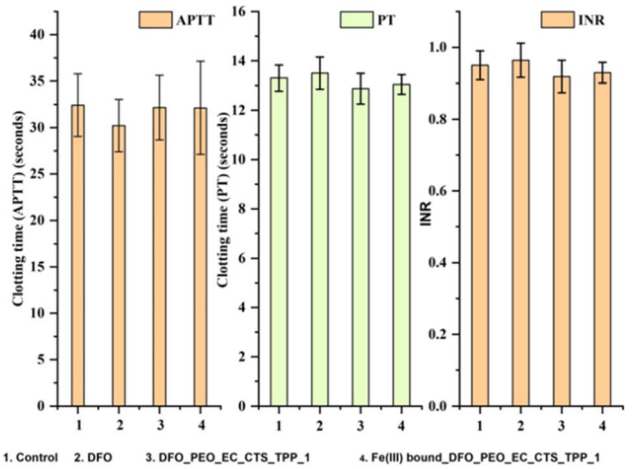

Fig. 13 Effect of DFO, DFO_PEO_EC_CTS_TPP_1 and Fe(III) bound DFO_PEO_EC_ CTS_TPP_1 on coagulation time. (Control: normal blood, final DFO concentration is 0.5 mg mL^{-1} at 37 °C).

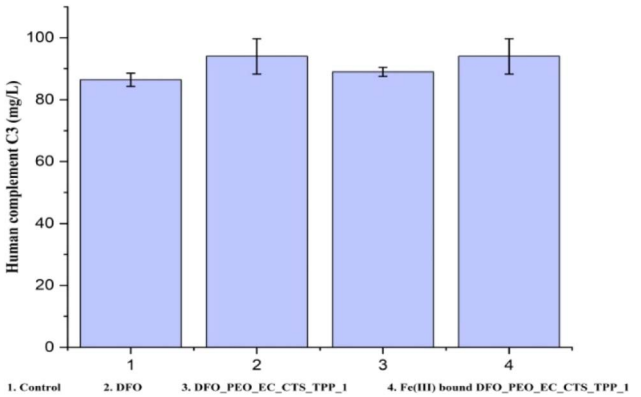

Fig. 14 Level of human complement C3 in the presence of normal blood, blood added with DFO, DFO_PEO_EC_CTS_TPP_1 and Fe(III) bound DFO_PEO_EC_CTS_TPP_1.

PT and APTT assay for blood coagulation. Evaluating of the effect of the newly modified drug on blood coagulation is crucial in order to form biocompatible a drug formulation. To assess the impact of nanocomposites on coagulation, PT and APTT

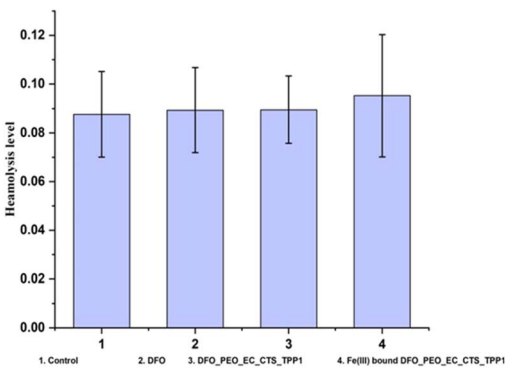

Fig. 15 Effect of drug on blood haemolysis.

assays were conducted using DFO, DFO_PEO_EC_CTS_TPP_1 and Fe(III) bound form of DFO_PEO_EC_CTS_TPP_1. PT was used to assess the effect of drug on extrinsic and common coagulation pathway.[39] While, APTT was used to evaluate the intrinsic and common coagulation pathway[39] by measuring the activated thromboplastin time.[40] The normal activated partial thromboplastin time is 22–40 seconds and if it exceeds more than the reference range, it reveals that the intrinsic coagulation pathway may get affected.[41] The PT reagent contains calcium rabbit brain thromboplastin and calcium chloride for initiating the coagulation process. The normal PT range is 10–14 seconds.[41] After adding PT/APTT reagents to DFO_PEO_EC_CTS_TPP_1 and Fe(III) bound form of DFO_PEO_EC_CTS_TPP_1 the coagulation times were measured and compared with that of DFO (Fig. 13). The results obtained for APTT, PT and INR are within the standard range and therefore, it can be concluded that these nanocomposite does not affect the blood coagulation pathways.

Human complement C3. Complement protein peptides are plasma proteins which upon activation induces histamine release or inflammatory reactions.[42] Therefore, determination of the extent of complement protein activation is worth in order

Table 8 IC 50 values of DFO, Fe_DFO_PEO_EC_CTS_TPP_1 and DFO_PEO_EC_CTS_TPP_1

System	IC50 (μM)	R^2
DFO	15.7 ± 3	0.8
Fe_DFO_PEO_EC_CTS_TPP_1	28.1 ± 4	0.7
DFO_PEO_EC_CTS_TPP_1	29.9 ± 5	0.9

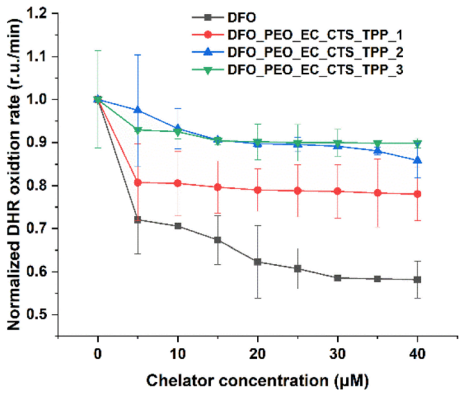

Fig. 17 Antioxidant assay in the Fe(II)/ascorbate system followed by DHR.

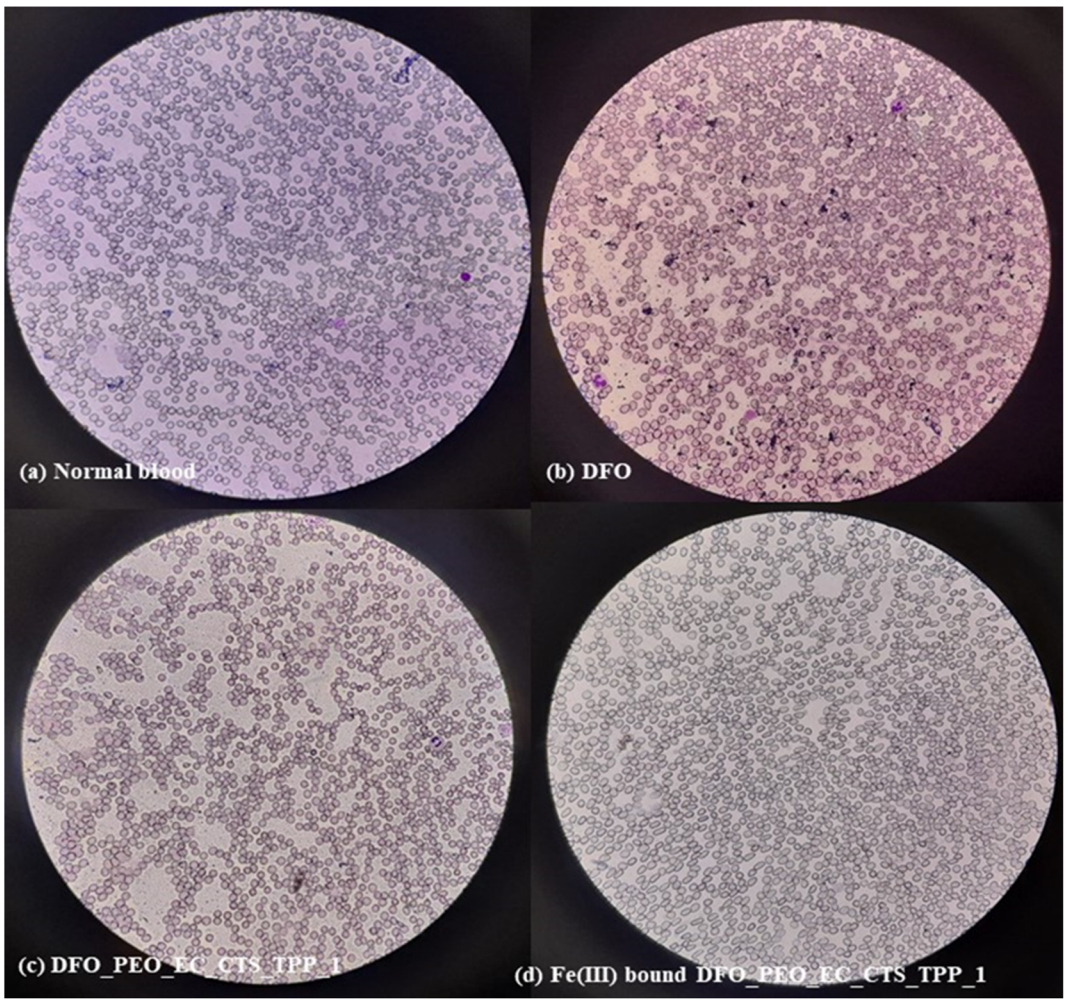

Fig. 16 Blood films of (a) normal blood, blood added with (b) DFO, (c) DFO_PEO_EC_CTS_TPP_1 and (d) Fe(III) bound DFO_PEO_EC_CTS_TPP_1.

Table 9 A summary of DFO encapsulation, cell permeability and release profile of some reported materials[a]

Reported materials	Blood compatibility/ cytocompatibility	Drug release profile at physiological (7.4) and intestinal pH values (5.8)	Cell permeability	Highest drug loading capacity	Drug entrapment efficiency	Mechanism of drug release and best fitting kinetic model	Nanoparticle diameter (nm)	Sustained release nature	References
DFO incorporated oligomeric proanthocyanidins nanoparticles (OPC-DFO NPs)	Heam compatible/ cytocompatible	N/R	Yes	N/R	N/R	N/R	148.6	N/R	13
DFO incorporated taurocholic acid conjugated hyaluronic acid (TCA9-HA-DFO)	Cytocompatible	N/R	Yes, assessed by using Caco-2 cells as a model for intestinal cell lines	N/R	N/R	N/R	71.38	N/R	12
poly(ethylene glycol)-based macromolecular based DFO	Heam compatible/ cytocompatible	N/R	N/R	15% DFO NMR	N/R	N/R	N/R	Yes	5
DFO in CMCS polymeric dispersions CMCS_TPP_DFO_25%	N/R	N/R	Yes	30%	N/R	N/R	335	Yes	17
CMCS_TPP_DFO_50%	N/R	N/R	Assessed by using murine	66.95%	N/R	N/R	265		17
CMCS_TPP_DFO_75%	N/R	N/R	RAW 264.7 macrophages or human HeLa cervical carcinoma cells with CMCS-DFO	92.2%	N/R	N/R	205		17
DFO loaded chitosan nanoparticle CS/TPP_20%DFO	N/R	N/R	Yes. Assesses by treatment of murine RAW 264.7 macrophages with nanoencapsulated DFO	11.55 ± 1.47	44.45 ± 1.39	Diffusion, linear driving force formula (LDF)	304 ± 25	N/R	15
CS/TPP_45%DFO	N/R	N/R	N/R	17.02 ± 2.12	26.15 ± 1.05		448 ± 31	N/R	15
CS/TPP_75%DFO	N/R	N/R	N/R	40.09 ± 4.22%	18.96 ± 0.89		528 ± 35	N/R	15
NPs encapsulating DFO were generated using the double emulsion method from mPEG-PLGA monomers	Cytocompatible	DFO is released more rapidly from the NPs at pH 4.4 than at pH 7.4	Yes. Assessed by using wild-type mice, as well as Hfe−/− and Hbbth3/+ mice	N/R	> 50%		105.3	Yes	45
Ultra-long circulating desferrioxamine based polymeric iron chelator (ULC-DFO)	Cytocompatible	N/R	Yes. Assessed by using human umbilical vein endothelial cells (HUVECs)	N/R	N/R	N/R	N/R	N/R	46
DFO_PEO_EC_CTS_TPP_1	Heamcompatible	DFO is released more rapidly from the composite at pH 7.4 than at pH 5.8	Yes. Assessed by using human cervical carcinoma (HeLa) cells line with DFO loaded PEO_EC_CTS_TPP_1	285.56 ± 0.04 mg g^{-1} (30%)	85.67 ± 13.35%	Case II relaxation mechanism, Peppas–Sahlin model at both pH 7.4 and 5.8	293.1 ± 52.9	Yes	This study

[a] N/R: not reported.

to analyze the biocompatibility of the modified drug. The human complement protein C3 is analyzed by reacting serum protein sample with anti-human complement anti serum at pH 7.4 in HEPEC buffer.[43] The turbidity induced by the formation of immune complexes was recorded at 340 nm using UV visible spectrophotometer. The C3 level was quantified upon exposure to DFO, DFO_PEO_EC_CTS_TPP_1 and Fe(III) bound DFO_-PEO_EC_CTS_TPP_1 (Fig. 14).

Repeated measure ANOVA (IBM SPSS statistic version 25), Wilks' Lambda test was performed to analyze whether or not the resulted PT, APTT and C3 protein values are significantly different. The Wilks' Lambda test comparison between control and DFO_PEO_EC_CTS_TPP_1 (DFO, 0.5 mg mL^{-1} at 37 °C) (APTT, p – 0.65, PT, p – 0.052, C3, p – 0.5), Fe(III) bound form of DFO_PEO_EC_CTS_TPP_1 added blood (APTT, p – 0.63, PT, p – 0.439,C3, p – 0.403) showed that the results are not significantly different at the p value of 0.05.

Red cell aggregation and haemolysis. The reaction of red blood cells to DFO, DFO_PEO_EC_CTS_TPP_1 and Fe(III) bound DFO_PEO_EC_ CTS_TPP_1 was monitored by analyzing the degree of haemolysis and blood film evaluation. The Fig. 15, depicts the haemolysis level of blood in the presence of DFO, DFO_PEO_EC_CTS_TPP_1 and Fe(III) bound DFO_PEO_EC_ CTS_TPP_1 and without adding any drug (control). Blood samples incubated with DFO did not show any visible colour change in the supernatant compared to that of normal blood. The degree of red colour present in supernatant was monitored at 510 nm using microplate reader. Repeated measure ANOVA (IBM SPSS statistic version 25), Wilks' Lambda test was used to study whether there is any significant difference between the haemolysis level of DFO and modified drug. The results indicated no significant differences in haemolysis level of normal blood, DFO and DFO_PEO_EC_CTS_TPP_1 and Fe bound form of DFO_PEO_EC_ CTS_TPP (p – 0.911 assuming 95% confidence interval).

Red cell aggregation was studied using an optical microscope and blood films pertaining to the normal blood and blood added with DFO, DFO_PEO_EC_CTS_TPP_1, Fe(III) bound DFO_PEO_EC_ CTS_TPP_1 are shown in Fig. 16. According to that, it was not observed any rouleaux formation and clumping was not observed, hence red cell aggregation was absent.

According to these results, it can be concluded that DFO encapsulated nanocomposites are biocompatible and do not affect blood coagulation, c3 complement protein pathways and do not induce blood hemolysis.

Cytotoxicity study using MTT assay. The determination of half maximally inhibitory concentration (IC50) is critical for assessing the cytotoxicity of the drug DFO and DFO encapsulated nanocomposite. The inhibitory effect of DFO, Fe_DFO_-PEO_EC_CTS_TPP_1 and DFO_PEO_EC_CTS_TPP_1 were assessed by using MTT based cell viability assay. The study successfully determined the IC50 values by using non-linear regression analysis with four parameter logistic model (GraphPad Prism, version 8) (Table 8).

The Fig. S6 shows the dose response curve for DFO, Fe_DFO_PEO_EC_CTS_TPP_1 and DFO_PEO_EC_CTS_TPP_1 nanocomposites. Encapsulation of DFO in PEO_EC_CTS_TPP matrix significantly increased the IC 50 value compared to neat DFO compound by – two-fold, suggesting its low cytotoxic effect.

Antioxidant activity. The ability of the chelator to prevent auto oxidation of ascorbate in the presence of iron(II) was measured (Fig. 17). This can occur by forming a stable six coordinated complex between DFO and iron or decreasing the $E^{\circ}_{Fe_{III}/Fe_{II}}$ to a greatly negative value.[44] According to the Fig. 17, DFO shows higher iron scavenging property and thereby higher antioxidant property. Compared to that, antioxidant property of all the DFO encapsulated nanocomposites is lower and maximum antioxidant property was shown by DFO_-PEO_EC_CTS_TPP_1. This is acceptable in a controlled release platform of DFO.

Stability of nanocomposites. The FTIR spectra of the initial DFO_PEO_EC_CTS_TPP_1 nanocomposite and after 24 months (Fig. S7) showed no significant differences, indicating chemical stability over the time. Additionally, the drug loading capacity of DFO_PEO_EC_CTS_TPP_1 nanocomposite after 24 months was found to be 248.12 ± 14.6, further supporting that the composite exhibits good stability under the storage conditions (−20 ± 5 °C).

The Table 9 shows a summary of heamcompatibility, and DFO release profile for some reported materials and compared to the available literature data, DFO-PEO-EC-CTS_1 composite shows the highest drug entrapment efficiency with anomalous drug release profile.

Conclusion

In this study, a nanoscale polymer blend (DFO_-PEO_EC_CTS_TPP) was developed to encapsulate the hydrophilic drug deferoxamine (DFO), aiming to enhance cell permeability and enable controlled drug release. The results showed that increasing the concentration of chitosan (CTS) in the nanocomposite (DFO_PEO_EC_CTS_TPP_1 > _2 > _3) led to higher drug loading capacity and entrapment efficiency, with PEO_EC_CTS_1 exhibiting the highest DFO encapsulsation. Additionally, DFO_PEO_EC_CTS_TPP_1 demonstrated the strongest antioxidant activity. The Peppas–Sahlin kinetic model best described the drug release behavior at both physiological pH (7.4) and intestinal pH (6.8), indicating a Case II relaxation mechanism, which supports sustained release over an extended period. A key limitation of the formulation was its high polydispersity, highlighting the need for optimization of particle size through adjustments in stabilizer concentration and homogenization time to achieve a more monodisperse system. *In vitro* hemocompatibility assays confirmed that the nanocomposite is biocompatible, while the formulation also showed good cellular permeability. These findings suggest that DFO-loaded PEO_EC_CTS_TPP nanocomposites offer a promising platform for pH-responsive, controlled DFO delivery, opening new avenues for future therapeutic applications.

Conflicts of interest

There are no conflicts of interest to declare.

Data availability

All experimental data supporting the findings of this study are available within the article and its supplementary information (SI). Supplementary information: additional raw data, including characterization datasets (SEM, XPS, PSA, FT-IR), drug loading and release profiles, and cytotoxicity assay results, are available from the corresponding author upon reasonable request. See DOI: **https://doi.org/10.1039/d5ra04417k**.

Acknowledgements

This work was supported by UNESCO-TWAS, Swedish International Development Cooperation Agency (Sida); FOM/RG/2022/07, FOM/RG/2023, FOM/RG/2024/2 and AHEAD-DOR-15 grants. The views expressed herein do not necessarily represent those of UNESCO-TWAS, Sida or its Board of Governors.

References

1 G. Jones, S. K. Goswami, H. Kang, H. S. Choi and J. Kim, *Nanomedicine*, 2020, **15**, 1341–1356.
2 P. H. Gary, J. B. McCormick, S. C. Trock, *et al.*, *N. Engl. J. Med.*, 1990, **323**, 1120–1123.
3 C. P. Holstege, *Encycl. Toxicol.*, 2005, 454–462.
4 R. A. Guilmette, E. A. Cerny and Y. E. Rahman, *Life Sci.*, 1978, **22**, 313–320.
5 N. A. A. Rossi, I. Mustafa, J. K. Jackson, H. M. Burt, S. A. Horte, M. D. Scott and J. N. Kizhakkedathu, *Biomaterials*, 2009, **30**, 638–648.
6 Blood Transfusion Therapy in β-Thalassaemia Major – Guidelines for the Clinical Management of Thalassaemia – NCBI Bookshelf, **https://www.ncbi.nlm.nih.gov/books/NBK173967/**, accessed 22 April 2022.
7 F. L. Cantrell, *Crit. Care Toxicol.*, 2016, 1–7.
8 E. C. P. Alta, D. Goswami, M. T. Machini, D. M. Silvestre, C. S. Nomura and B. P. Espósito, *BioMetals*, 2014, **27**, 1351–1360.
9 E. H. Lau, E. A. Cerny and Y. E. Rahman, *Br. J. Haematol.*, 1981, **47**, 505–518.
10 S. P. Young, S. P. Young, E. Baker and E. R. Huehns, *Br. J. Haematol.*, 1979, **41**, 357–363.
11 K. Elumalai, S. Srinivasan and A. Shanmugam, *Biomed. Technol.*, 2024, **5**, 109–122.
12 E. O. Agboluaje, S. Cui, N. J. Grimsey and M. P. Xiong, *AAPS J.*, 2024, **26**, 1–14.
13 F. Zhu, J. Zhang, J. Zhong, T. Wang, Y. Li and Z. Gu, *J. Controlled Release*, 2023, **356**, 84–92.
14 K. Sonaje, K. J. Lin, M. T. Tseng, S. P. Wey, F. Y. Su, E. Y. Chuang, C. W. Hsu, C. T. Chen and H. W. Sung, *Biomaterials*, 2011, **32**, 8712–8721.
15 M. Lazaridou, E. Christodoulou, M. Nerantzaki, M. Kostoglou, D. A. Lambropoulou, A. Katsarou, K. Pantopoulos and D. N. Bikiaris, *Pharmaceutics*, 2020, **12**, 238.
16 S. Vignesh, A. Sivashanmugam, M. Annapoorna, R. Janarthanan, I. Subramania, N. Shantikumar V. and R. Jayakumar, *Colloids Surf., B*, 2018, **161**, 129–138.
17 G. Michailidou, Y. Li, A. Zamboulis, G. Karlioti, D. Meimaroglou, K. Pantopoulos and D. N. Bikiaris, *Int. J. Mol. Sci.*, 2024, **25**(2), 913–933.
18 Medicines and Healthcare Products Regulatory Agency, *British Pharmacopoeia 2009 Volume III Desferrioxamine Injection*, 2009.
19 R. Enayatifard, M. Saeedi, J. Akbari and Y. H. Tabatabaee, *Trop. J. Pharm. Res.*, 2009, **8**, 425–432.
20 V. U. Godakanda, H. Li, L. Alquezar, L. Zhao, L. M. Zhu, R. de Silva, K. M. N. de Silva and G. R. Williams, *Int. J. Pharm.*, 2019, **562**, 172–179.
21 S. Dash, P. N. Murthy, L. Nath and P. Chowdhury, *Acta. Pol. Pharm.–Drug Res.*, 2010, **67**, 217–223.
22 D. C. Manatunga, V. U. Godakanda, R. M. Silva and K. M. N. Silva, *Wiley Interdiscip. Rev.:Nanomed. Nanobiotechnol.*, 2019, DOI: **10.1002/wnan.1605**.
23 M. L. Bruschi, *Strategies to Modify the Drug Release from Pharmaceutical Systems*, 2015, 63–86.
24 A. Gupta, J. Bhasarkar, M. R. Chandan, A. H. Shaik, B. Kiran and D. K. Bal, *J. Macromol. Sci., Part B:Phys.*, 2020, **59**, 713–730.
25 F. Langenbucher, *J. Pharm. Pharmacol.*, 1972, **24**, 979–981.
26 N. A. Peppas and J. J. Sahlin, *Int. J. Pharm.*, 1989, **57**, 169–172.
27 R. B. Baggi and N. B. Kilaru, *Asian J. Pharm. Technol.*, 2016, **6**, 223.
28 S. A. A. Rizvi and A. M. Saleh, *Saudi Pharm. J.*, 2018, **26**, 64–70.
29 J. J. Yeh and I. Lindau, *At. Data Nucl. Data Tables*, 1985, **32**, 1–155.
30 M. P. Seah and W. A. Dench, *Surf. Interface Anal.*, 1979, **1**, 2.
31 K. R. Koswattage, I. Shimoyama, Y. Baba, T. Sekiguchi and K. Nakagawa, *J. Chem. Phys.*, 2011, **135**, 2.
32 K. R. Koswattage, I. Shimoyama, Y. Baba, T. Sekiguchi and K. Nakagawa, *Appl. Surf. Sci.*, 2011, **258**, 1561–1564.
33 M. S. Fernando, A. K. D. V. K. Wimalasiri, K. Dziemidowicz, G. R. Williams, K. R. Koswattage, D. P. Dissanayake, K. M. N. de Silva and R. M. de Silva, *ACS Omega*, 2021, **6**, 8530.
34 D. Q. Muheddin, S. B. Aziz and P. A. Mohammed, *Polymers*, 2023, **15**(3), DOI: **10.3390/polym15030771**.
35 S. M. Fernando, A. K. D. V. K. Wimalasiri, K. Dziemidowicz, G. R. Williams, K. Rasika Koswattage, D. P. Dissanayake, K. M. Nalin De Silva and R. M. De Silva, *R. Soc. Open Sci.*, 2023, DOI: **10.1098/RSOS.221514**.
36 P. Bhadra, M. S. Shajahan, P. N. Patel, E. Bhattacharya, A. Chadha and P. K. Sekhar, *J. Electrochem. Soc.*, 2018, **165**, B3017–B3022.
37 S. De Silva and C. S. Rajapakse, in *Proceedings of the Research Symposium of Uva Wellassa*, University, 2015.
38 J. Siepmann, R. A. Siegel and M. J. Rathbone, *Fundamentals and Applications of Controlled Release Drug Delivery*, 2012, 1–594.

39 Sang Medicine, Screening Tests in Haemostasis: The APTT, **https://practical-haemostasis.com/Screening-Tests/aptt.html**, accessed 31 July 2024.
40 K. L. Epstein, *Robinson's Curr. Ther. Equine Med*, 7th edn, 2015, 500–502.
41 S. M. Bates and J. I. Weitz, *Circulation*, 2005, **112**(4), DOI: **10.1161/circulationaha.104.478222**.
42 R. J. Gobel, J. Janatova, J. M. Googe and D. J. Apple, *Biomaterials*, 1987, **8**, 285–288.
43 Randox, Complement C3 | Biochemistry | Reagent | Randox Laboratories, **https://www.randox.com/complement-c3/**, accessed 4 August 2024.
44 G. S. da Silva, Z. Shang, P. Kalansuriya, R. J. Capon and B. P. Espósito, *BioMetals*, 2019, **32**, 707–715.
45 S. Guo, G. Liu, D. M. Frazer, T. Liu, L. You, J. Xu, Y. Wang, G. J. Anderson and G. Nie, *Nano Lett.*, 2018, **18**, 5782–5790.
46 J. L. Hamilton, M. Imran ul-haq, S. Abbina, M. T. Kalathottukaren, B. F. L. Lai, A. Hatef, S. Unniappan and J. N. Kizhakkedathu, *Biomaterials*, 2016, **102**, 58–71.